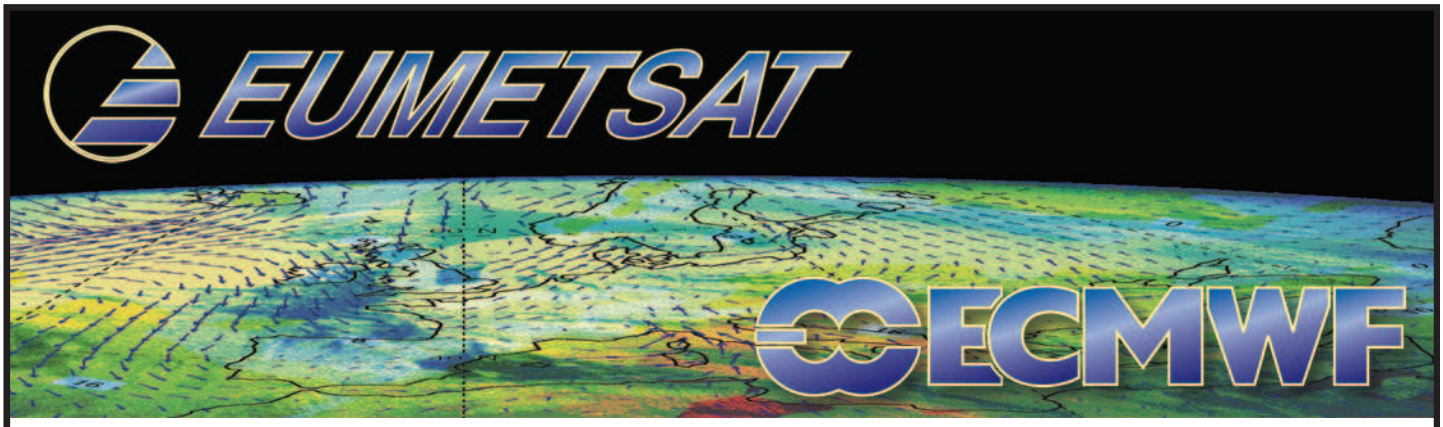

EUMETSAT/ECMWF Project Report

Optimising Tracking Strategies for Radio Occultation. Task 1 - the profile dataset

S. B. Healy

March 19, 2012

A full list of ECMWF Publications can be found on our web site under:
http://www.ecmwf.int/publications/

Contact: library@ecmwf.int

European Centre for Medium Range Weather Forecasts
Shinfield Park, Reading, RG2 9AX, England

Summary

This report summarizes progress on task 1 of the "Optimising Tracking Strategies for Radio Occultation" project. Fifty-five refractivity one-dimensional (1D) profiles and two-dimensional (2D) slices at measurement locations have been selected, for use in realistic wave optics simulations of GPS radio occultation measurements. The dataset include some cases of challenging measurement conditions, such as severe multipath and de-focusing of the signal. The 1D profiles have been assigned a category number between 1 and 4. Category 1 profiles are considered to be the easiest measurement conditions and category 4 are the most difficult. The category value of a profile is determined by the maximum refractivity gradient above 100 m. The probability density functions of the maximum refractivity gradients, and the geographical distributions of the four categories, are presented. The results with 1D profiles indicate that the most challenging atmospheric conditions for GPS radio occultation measurements are cases of low cloud cover at low latitudes. In contrast, convective conditions appear to produce relatively smooth profiles, which should be straightforward to measure.

The 2D dataset enables the impact of horizontal refractivity gradients to be investigated.

1 Introduction

When making GPS radio occultation measurements it is known that some atmospheric conditions produce complex signal dynamics, which can be difficult for the GPS receivers to track. It is important to test GPS receiver performance in these situations, in order to have an understanding of the measurement errors. The aim of task 1 of this study is to derive a set of refractivity one-dimensional (1D) profiles and two-dimensional (2D) slices from ECMWF model output, for use in realistic wave optics simulations of radio occultation events. These simulated observations can be used to test GPS receiver models.

ECMWF has tried to include a reasonable number of "challenging" profiles in the dataset. These include cases where vertical gradients in the water vapour produce severe multipath and de-focusing, and conditions that lead to ducting of the signals. ECMWF does not have a wave optics forward model, so we have used simplified geometrical optics bending angle models to help identify these interesting cases.

The dataset contains 55 cases [1]. Each 1D profile has been assigned a "category" between 1 and 4: category 1 is considered the most straightforward measurement conditions, and category 4 is the most difficult. The probability of finding each 1D category, and their geographical distributions has been investigated. The results suggest that the most challenging measurement conditions are cases of low cloud in the tropics, rather than cases with where the vertically integrated moisture is largest.

The 2D slices provide information on which cases are likely to be affected by horizontal gradients. We suggest using the variation of the impact parameter along the ray path as a means of identifying such cases.

Clearly, the value of this dataset depends on how physically realistic the profiles derived from the ECMWF output are, and in particular the representation of the planerary boundary layer (PBL) and low cloud, because these can lead to difficult measurement conditions. The paramatrization of the dry boundary layer and stratocumulus in the ECMWF model is described by Köhler *et al.* (2011) and comparisons against observations are presented by Hannay *et al.* (2009) and Wyant *et al.* (2010). ECMWF generally performs well in comparisons with obser-

[1] There are actually only 54 cases because of an error which means Case 40 and Case 49 are identical (See appendix)

vations, when compared with other models. For example, Hannay *et al.* (2009) state that the ECMWF model produces the best results in terms of the PBL height an mixing for the "East Pacicific Investigation of Climate" (EPIC) measurement campaign.

The 1D profile selection process is outlined in section 2. In section 3, we suggest four categories of 1D profile, and present an example of each category. The probability density functions of the maximum refractivity gradients and the spatial distribution categories are presented section 4. The corresponding 2D slices will be discussed in section 5, and the concluding remarks are given in section 6.

2 Profile selection

This section describes the 1D profile selection. The profiles are derived from operational short-range forecasts produced with the ECMWF Integrated Forecast System (IFS) CYCLE 36R1. This has a spectral resolution of T1279 in the horizontal, with 91 levels in the vertical, from the surface up to 0.01 hPa.

Using 1D profiles in simulations studies is clearly a simplification, but it has the advantage of removing retrieval errors caused by horizontal gradients from the inverse problem, and it should be possible to invert the simulated bending angles with an Abel transform, to recover the original refractivity profile. This provides a useful consistency test for the simulations. Cases where horizontal gradients are likely to have a significant impact will be discussed in section 5.

It seems reasonable to assume that the most difficult measurement conditions are caused by large gradients of water vapour producing complex signal dynamics (e.g. Sokolovskiy, 2003), and the selection methodology has been based on this assumption. We have selected 55 cases listed in the Appendix. Many of the profiles will produce complex simulated observations, but a number of easier cases have also been included for calibration purposes. These include measurements in polar regions and over deserts,where the water vapour content is low.

The 55 cases have been chosen by looking at maps of GRAS and COSMIC observation locations superimposed on the following fields produced by the model:

- low cloud cover
- total precipitable water
- rain rate integrated over a six hour window
- convective available potential energy
- surface pressure

The observation locations used in this work are the "representative" locations given in the header of operational BUFR files, and no attempt has been made to include tangent point drift.

An example of the maps used to identify interesting cases is given in Figures 1 and 2 for July 22, 2010. These show the GRAS (squares) and COSMIC (circles) observation locations superimposed on the NWP fields. For example, CASE 42 was selected (`CASE_42_alpha_20100722_112647.dat`) using these figures because it was situated in a region of low cloud cover (latitude(lat)=-33.9 (degrees), longitude(lon)=54.6 (degrees)) [2].

[2] All latitudes and longitudes will be given in degrees in this report. The latitudes range from 90 degrees to -90 degrees. The longitudes range from 180 degrees to -180 degrees, with a negative value denoting west of 0 degrees longitude.

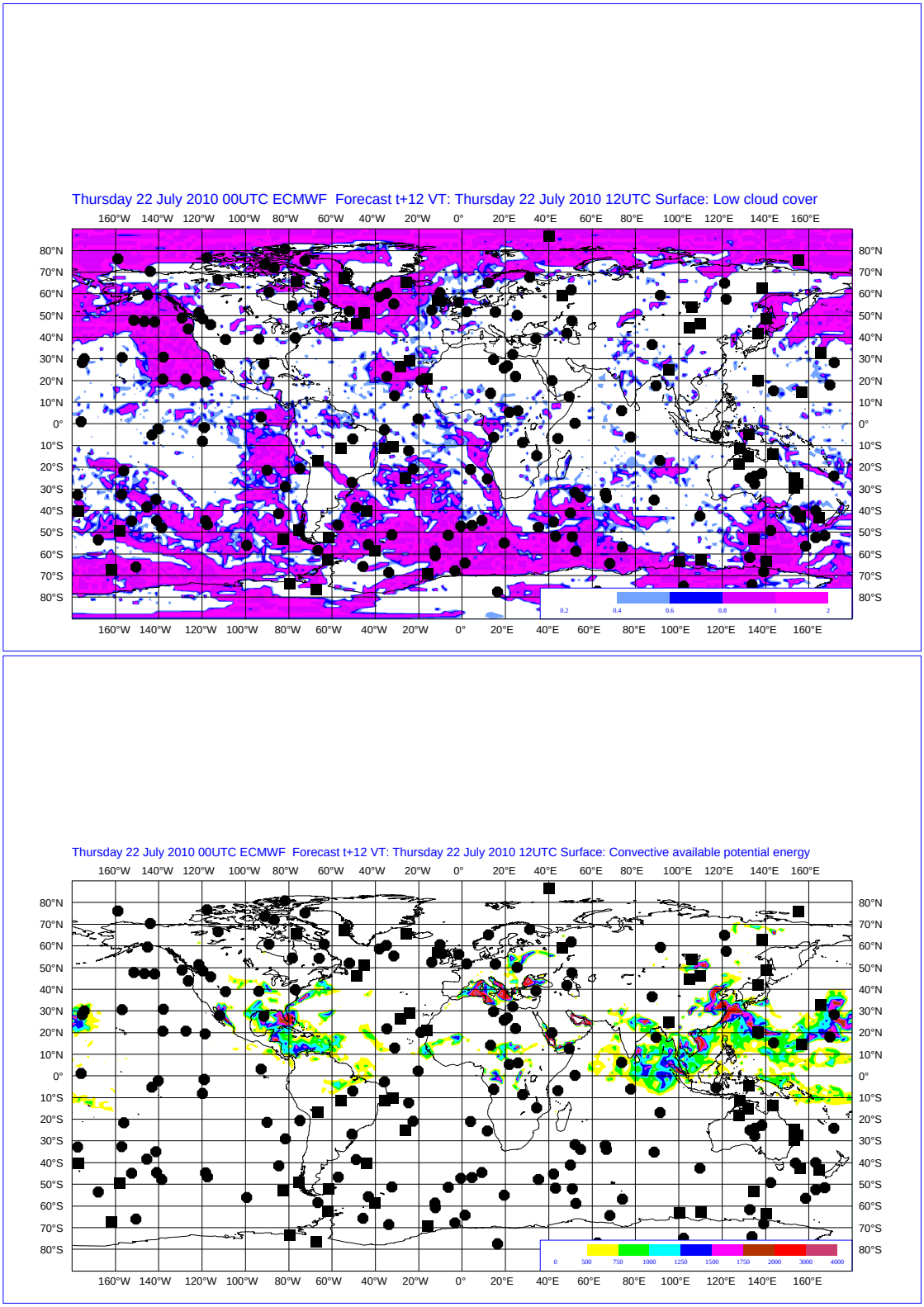

Figure 1: The GRAS (squares) and COSMIC (circles) observations superimposed on the (upper) NWP model low cloud fraction and (lower) Convective Available Potential Energy (J/kg). The cloud fraction is a scalar between 0 and 1, denoting the fraction of the grid-box covered in cloud.

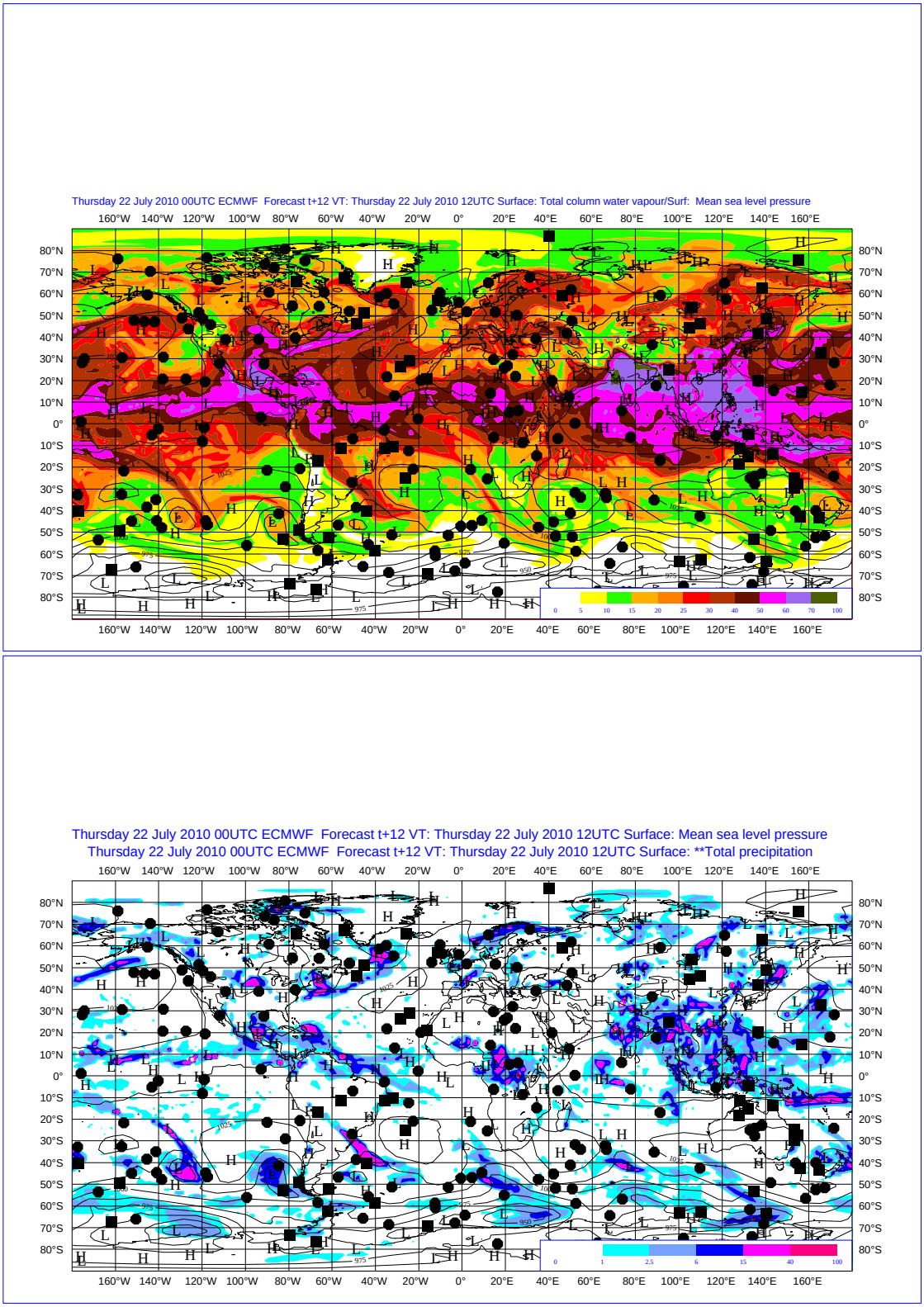

Figure 2: The GRAS (squares) and COSMIC (circles) observations superimposed on the (upper) NWP model total column water vapour (kg/m^2) and (lower) total precipitation (mm) accumulated over 6 hours. The plots also shows the surface pressure map (hPa).

Once an interesting case has been identified, the one-dimensional NWP profile information is extracted on the 91 model levels between the surface and 0.01 hPa at the observation location. The refractivity on the model levels is defined as

$$N = \frac{77.6P}{T} + \frac{3.73 \times 10^5 e}{T^2}. \tag{1}$$

where P, T and e are the model pressure, temperature and vapour pressure, respectively.

The bending angles are calculated by evaluating the standard bending angle integral with the ROPP 1D operator approach (Healy and Thépaut 2006)

$$\alpha(a) = -2a \int_a^\infty \frac{\frac{d \ln n}{dx}}{(x^2 - a^2)^{1/2}} dx \tag{2}$$

where α is the total ionospheric-corrected bending angle (radians), n is the refractive index derived from the model and $x = nr$, where r is the radius value of a point on the ray-path. The bending angle observation operator only assumes a continuous refractivity profile – refractivity varying exponentially between the model levels – but does not assume continuous refractivity gradients across the model level boundaries. Note that having continuous refractivity gradients is a standard assumption in wave optics forward models, because wave optics calculations require the second derivative of the refractivity profile. The simulated bending angles produced with the 1D operator are available as part of the profile dataset, so the implications of these different assumptions can be tested.

Bending angles are calculated with an impact parameter separation of 25 m, from the surface to 20km. This vertical sampling is used in order to investigate possible multipath, de-focusing, and the arrival times for the the simulated bending angles. The de-focusing factor (Haugstad, 1978), DF, is proportional to the gradient of the bending angle with respect to the impact parameter,

$$DF \propto \frac{1}{1 - l \partial \alpha / \partial a} \tag{3}$$

assuming the distance between the tangent point and the LEO is $l = 3300km$. The de-focusing factor is useful, but it can be noisy and difficult to interpret. An alternative approach is to use the bending angle arrival times can be estimated from the measurement geometry. For the purpose of this calculation, we assume circular orbits with representative values for the radius and velocities of the GPS and LEO satellites. The GPS radius and velocities are $r_t = 26600km$ and $v_t = 3.9kms^{-1}$, and the corresponding LEO values are $r_r = 7015km$ and $v_r = 7.5kms^{-1}$. For convenience we assume that the satellites move in opposite directions, but this is just a convention, because the observation operator used to simulate the bending angles makes no distrinction between rising and setting occultations, and this assumption does not affect the interpretation of the arrival times.

From geometrical considerations, the bending angle (in radians) can be written as

$$\alpha(a) = \theta + \sin^{-1}(a/r_t) + \sin^{-1}(a/r_r) - \pi \tag{4}$$

enabling θ – the angle between the satellites – to be calculated. We can then estimate the arrival time by dividing the angular separation, θ, by the angular velocity

$$t_a = \frac{\theta}{v_t/r_t + v_r/r_r} - t_{20} \tag{5}$$

where t_{20} is an arbitrary constant, usually taken to be time calculated for an impact height of 20 km.

Plotting $\alpha(t_a)$ at the 25 m impact height sampling rate is particularly useful because it provides an indication of multipath, when more than one ray arrives at the receiver for a given t_a. It also highlights where signal

de-focusing is likely to lead to low amplitudes at the receiver, if we interpret the time separation between consecutive points as being related to the energy in the signal reaching the receiver at that time. Some examples are given in section 3, and see Figure 10 in particular for an example of multipath and de-focusing.

3 Suggested Categories

Each 1D profile in the dataset has been assigned a "category" value between 1 and 4. The category value is determined by maximum refractivity gradient above 100 m; the statistics of this parameter, including the probability density functions as a function of area and season, are given in section 4.

The maximum refractivity gradient indicates how difficult it will be to make a measurement, because large gradients produce multipath and de-focusing of the signal. The 100 m lower limit is used to screen out surface ducts.

The four categories used are:

- **Category 1** (Standard): The maximum refractivity gradient above 100 m is less than half that required for ducting $(-)dN/dz \leq 0.157/2$ (N units m^{-1})
- **Category 2** (Intermediate): Maximum refractivity gradient above 100 m is $0.157/2 < (-)dN/dz \leq 0.1$(N units m^{-1})
- **Category 3** (Challenging): Maximum refractivity gradient above 100 m is $0.1 < (-)dN/dz \leq 0.157$ (N units m^{-1})
- **Category 4** (Elevated Duct): The maximum refractivity gradient above 100 m is $(-)dN/dz > 0.157$ (N units m^{-1})

An example for each category taken from the 1D profile data set will now be given.

3.1 Category 1

CASE 3 (`CASE_03_ref1d_20100701_114419.dat`) is a GRAS measurement located in Antarctica (lat=-83.4,lon=81.2) on July 1, 2010 at 11.44 UTC. The occultation stops at an impact height of 3.5 km because of the height of the orography over Antarctica. The profile contains a surface duct, and this is an example of a situation which would have been classified as category 4, had it not been for the 100 m limit when searching for the maximum gradient. Figure 3 shows the refractivity derived for CASE 3. The refractivity values are low, because the profile is extremely cold and dry. In fact the maximum refractivity value is only 213 N units. The bending angle as function of impact parameter is shown in Figure 4. The bending angle values are low, and there are no features that would lead to significant multipath or de-focusing. In summary, there are no obvious reasons why the CASE 3 conditions would be difficult to measure, and it should be used to calibrate more difficult cases.

Another interesting example of a category 1 profile is CASE 51 (See Appendix). In this instance, a GRAS measurement is located near the centre of the model representation of Hurricane IGOR. The surface pressure is 978 hPa, and the profile is very moist producing a refractivity value at the surface of 392 N units, but the refractivity and bending angle profiles are remarkably smooth.

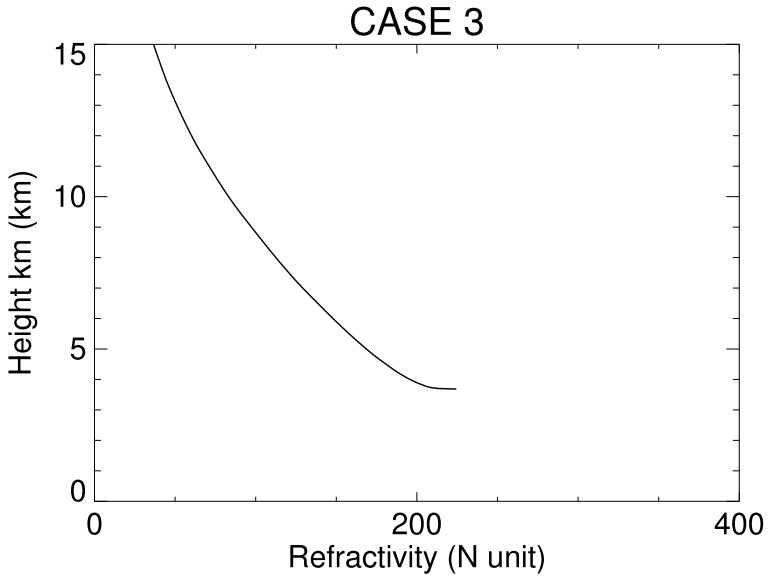

Figure 3: The refractivity profile for CASE 3.

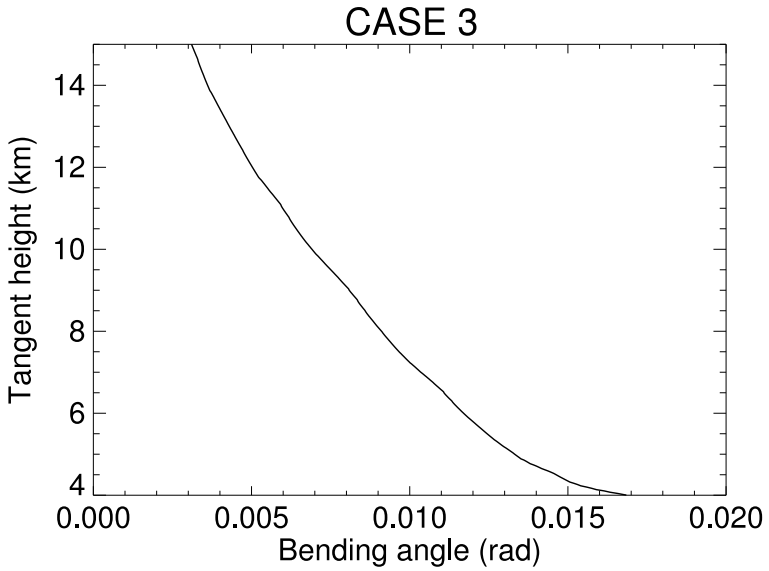

Figure 4: The bending angle as a function of impact parameter for CASE 3.

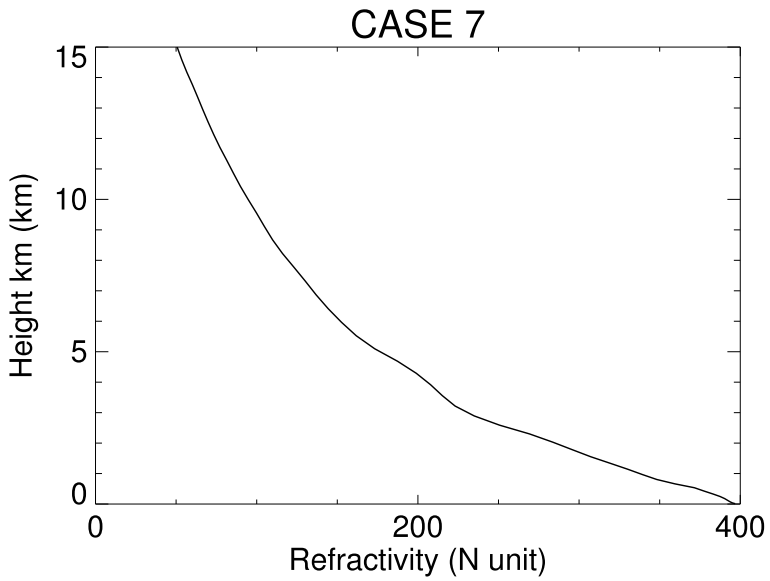

Figure 5: The refractivity profile for CASE 7.

3.2 Category 2

CASE 7 (`CASE_07_ref1d_20100701_121607.dat`) is a GRAS measurement located near Taiwan (lat=21.4,lon=121.1) on July 1, 2010 at 12.16 UTC. It contains high levels of water vapour, and this results in a high value of refractivity at the surface of $\sim$ 395 N units. However, the refractivity profile is quite smooth (Figure 5), and the bending angle profile is reasonably straightforward (Figures 6 and 7). This is an example of a case where extremely high water vapour content does not imply particularly difficult measurement conditions.

3.3 Category 3

CASE 12 (`CASE_12_ref1d_20100701_235317.dat`) is a COSMIC-5 measurement located at (lat=-6.4,lon=-85.9) on July 1, 2010 at 23.53 UTC. The location has low cloud, and the maximum refractivity gradient is 0.137 N units m^{-1} about 1.8 km above the surface. The humidity profile decreases rapidly across the temperature inversion at the top of the cloud, but then increases again and this leads to conditions where refractivity increases with height (see Figure 8). The refractivity profile produces a very challenging bending angle profile, as shown Figure 9. The largest bending angle is greater than 0.05 rad, and the bending angle vertical gradients are large, implying significant de-focusing. Plotting the bending angle as a function of arrival time is instructive, as shown in Figure 10. More than one ray arrives between 12 s to 15 s, implying significant multipath. There is a gap between $\sim$ 22 s to 28 s suggesting a low amplitude at the receiver, and then the signal returns. The gap is associated with bending angles which have a tangent height near the maximum refractivity gradient, because of atmospheric defocusing of the signal. An alternative way to look at this is that the large refractivity gradients produce large bending angle values, which must arrive late in the measurement, when the signal to noise is low, because of the measurement geometry.

In CASE 12, an obvious question is whether the bending angles arriving after 40 s are measurable, or are they lost because of low signal to noise? It should be emphasised that this is not a multipath issue that can be overcome with a retrieval based on wave optics. Simple geometrical considerations mean that these large bending angles arrive late at the receiver (or, equivalently, with low Straight Line Tangent Altitude) and they

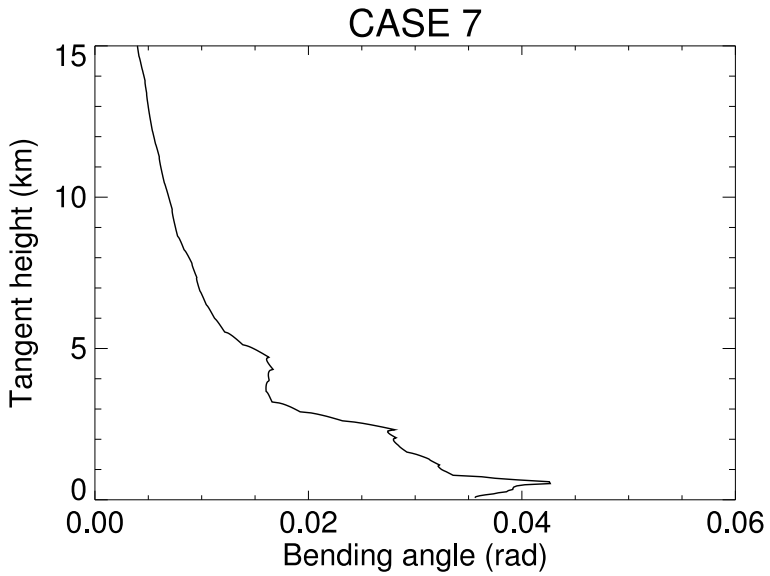

Figure 6: The bending angle as a function of impact parameter for CASE 7.

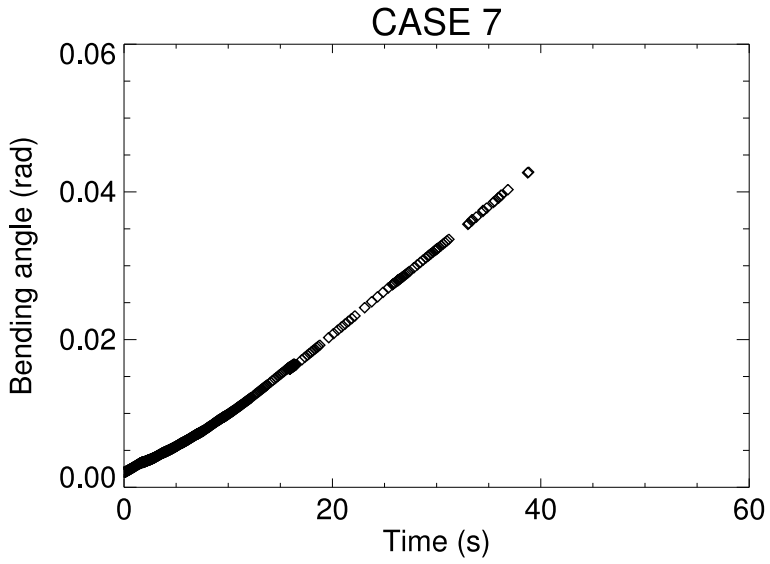

Figure 7: The bending angle as a function of arrival time for CASE 7.

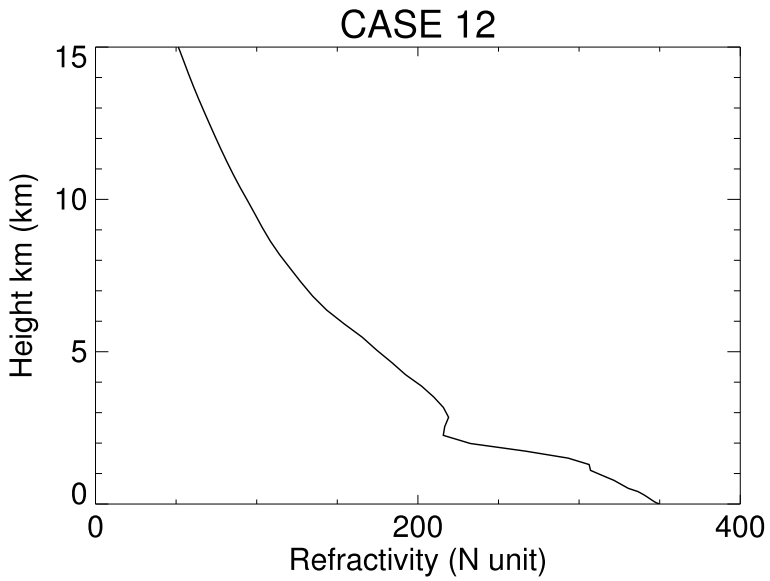

Figure 8: The refractivity profile for CASE 12.

have low amplitude, so they are difficult to measure.

3.4 Category 4

CASE 5 (`CASE_ref1d_20100701_235317.dat`) is located at (lat=-29.06,lon=-75.8) on July 1, 2010 at 11.59 UTC. The profile has a ducting layer near 1 km above the surface (see Figure 11). The ducting layer is caused by the reduction of water vapour across a temperature inversion. Ducting layers produce a singularity in the 1D bending angle integral (the ray bending tends to infinity, and therefore the arrival time tends to infinity) and it is not possible to calculate the bending angles below such a layer with the 1D operator. Consequently, the bending angle calculation stops (Figure 12), suggesting the loss of signal. Note how the separation between the bending angle arrival times increases in Figure 13 before the signal is lost. We are not able to say anything useful about the signal at the receiver emerging from below the ducting layer using this simplified approach, but wave optics codes show that some signal can emerge from below such a layer.

Studies suggest that the well known refractivity bias in the tropics occurs primarily in regions of semi-permanent stratocumulus that produce ducting conditions (Xie *et al.* 2010, Von Engeln and Teixeira 2004).

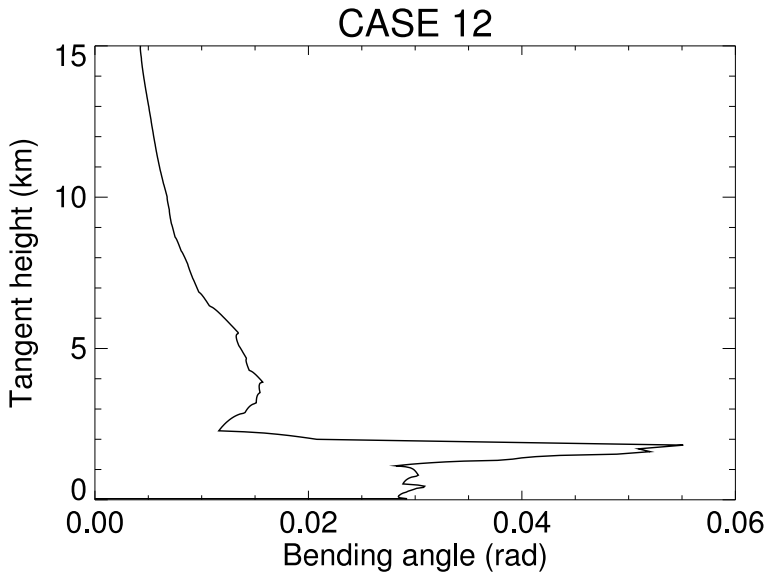

Figure 9: The bending angle as a function of impact parameter for CASE 12.

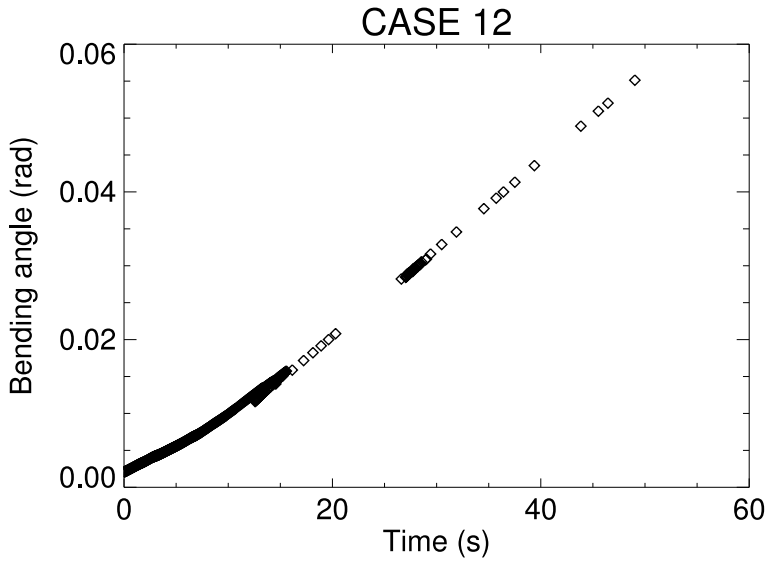

Figure 10: The bending angle as a function of arrival time for CASE 12.

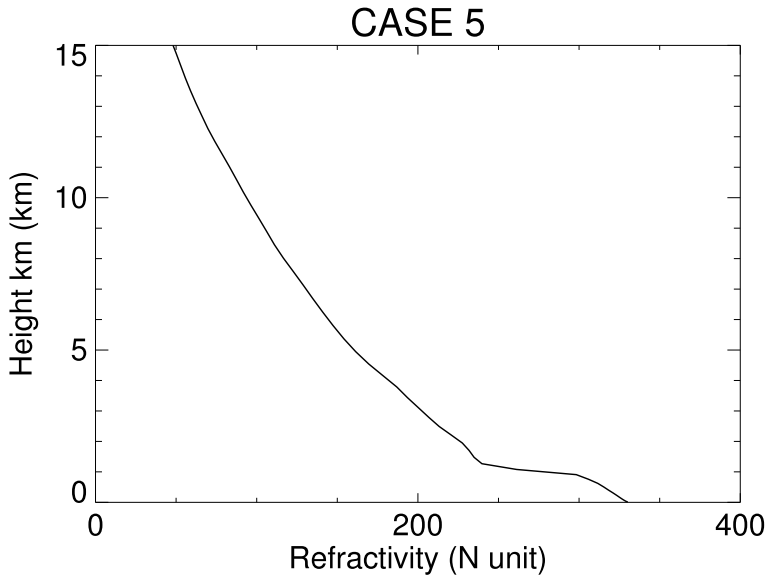

Figure 11: The refractivity profile for CASE 5.

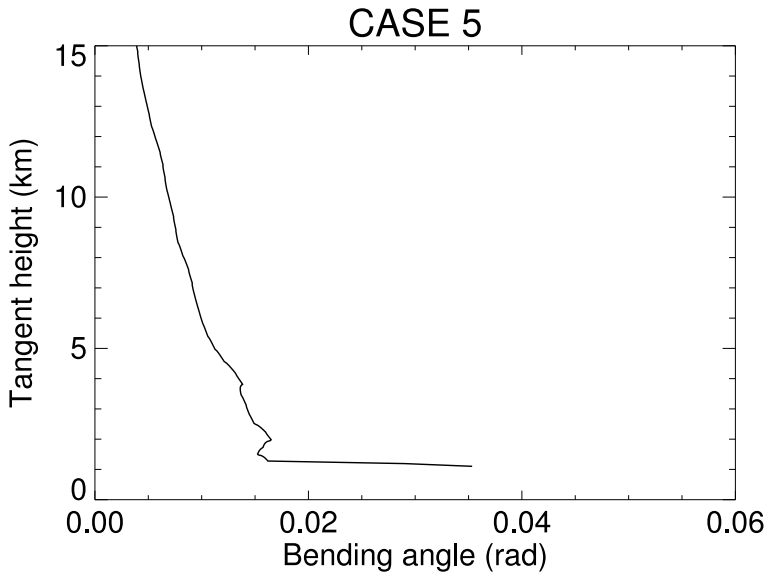

Figure 12: The bending angle as a function of impact parameter for CASE 5.

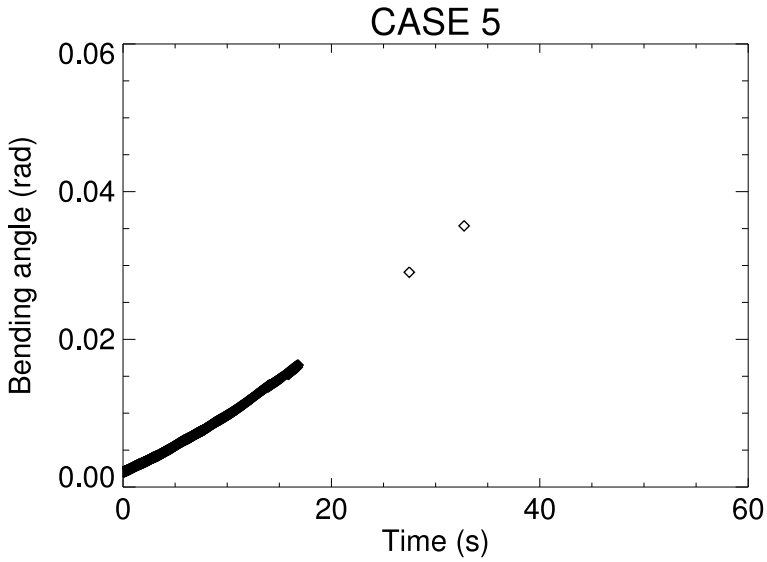

Figure 13: The bending angle as a function of arrival time for CASE 5.

Table 1: The globally averaged probability of occurrence of the four categories of refractivity gradient (given as a percentage), for the four seasons covering the period December 1, 2009 to November 30, 2010.

Season	Category 1	Category 2	Category 3	Category 4
DJF	47.7	16.1	22.9	13.3
MAM	45.4	16.7	24.5	13.4
JJA	43.4	18.0	25.5	13.1
SON	44.6	17.2	25.1	13.1

4 Probability density functions of the maximum refractivity gradients

The probability density functions (PDFs) of the maximum radial refractivity gradients produced by the ECMWF model have been estimated as a function of season and region. These PDFs are useful because they indicate how frequently the challenging measurement conditions are likely to occur. The results presented here suggest that the frequency of category 3 and category 4 profiles is significant.

The PDFs have been derived for the four seasons DJF, MAM, JJA and SON for the period December 1, 2009 to November 30, 2010. They have been generated by sampling 500 hundred random locations on the earth at 00Z and 12Z each day, resulting in 1000 sampled locations per day.

Table 1 summarises the percentage of each category found for each of the seasons and the corresponding PDFs of the maximum gradient are shown in Figure 14. The challenging category 3 and category 4 profiles account for around 24 % and 13 % of the samples, respectively, in each season. It is also found that in 7 % of the cases refractivity increases with height, as a result of a double peak in the humidity profiles. These profiles are likely to produce considerable multipath, because of the large change in the refractivity gradient with height (multipath is related to the second derivative of the refractivity profile). In addition, they are not well handled in the ROPP observation operators where a negative gradient is assumed.

A breakdown into the latitude bands for DJF is shown in Figure 15 (We will only show the DJF plot in detail in the remainder of this section, but the main conclusions are equally valid for other seasons). The largest gradients tend to be found in the tropics, and consequently the mode of the PDF is clearly shifted to higher values. It also is evident that warmer, moister conditions in the summer hemisphere tend to produce larger refractivity gradients, meaning that the gradients in the southern hemisphere are larger than in the northern hemisphere for DJF. However, it does not seem follow that the largest refractivity and bending angle gradients are correlated with the largest column integrated water vapour values. In fact, from a 1D profile perspective, these results suggest that regions associated with high column integrated water vapour and large scale convection tend to produce reasonably smooth refractivity profiles, which should be relatively easy to measure.

Figure 16 shows the distribution of category 1 and category 2 points for the DJF season, superimposed on the total precipitation produced by the model, averaged over the season (Superimposing on to the average column integrated water vapour would produce a similar picture qualitatively). Each point is the location of a category 1 or category 2 profile on the respective plot. The category 1 points tend to be found in the cold and dry regions at the higher latitudes, and there is a higher density in the winter hemisphere. However, there is a clear pattern in the distribution of the category 1 points in the tropics, where they tend to be found at the ITCZ, and generally where there are high moisture levels and precipitation. Category 1 profiles in the tropics are associated with convection, and conversely they do not appear in regions of low cloud produced by large scale descent. Category 2 points have a lower density than category 1 at high latitudes, but follow the same general pattern in the tropics, being found in convective regions, but not in regions of large scale descent.

Figure 17 shows the spatial distribution of the category 3 and category 4 profiles, superimposed on the the model low cloud fraction, averaged over DJF. The more challenging conditions occur mainly at low latitudes. The category 3 profiles are distributed more evenly, with the category 4 profiles primarily occurring in regions of semi-permanent low cloud, off the west coast of the continents. In DJF, for cloud-fractions ≥ 0.95 in the tropics, the probability of encountering a category 3 or category 4 profile increases to 24.1 % and 32.2 %, respectively (compare with values given Table 1). Furthermore, category 4 profiles are notably absent from the ITCZ region. These results confirm the picture that convection produces smooth vertical profiles that are relatively easy to measure, whereas the refractivity profiles produced in regions of large scale descent can be problematic for GPS-RO. We can illustrate this by plotting the PDFs for two regions in the same latitude band in the Tropics. Area 1 is a low cloud region and it is defined by (-10 $\geq$ lat $\geq$ -20) and (-80 $\geq$ lon $\geq$ -100). Area 2 is convective region defined as (-10 $\geq$ lat $\geq$ -20) and (-160 $\geq$ lon $\geq$ -180). The PDFs are illustrated in Figure 18. They are much noisier than earlier PDF plots because the sample number is only $\sim$ 450, but they clearly illustrate how the measurement conditions encountered in a given latitude band in the tropics can differ considerably as a result of the underlying climatology of the region.

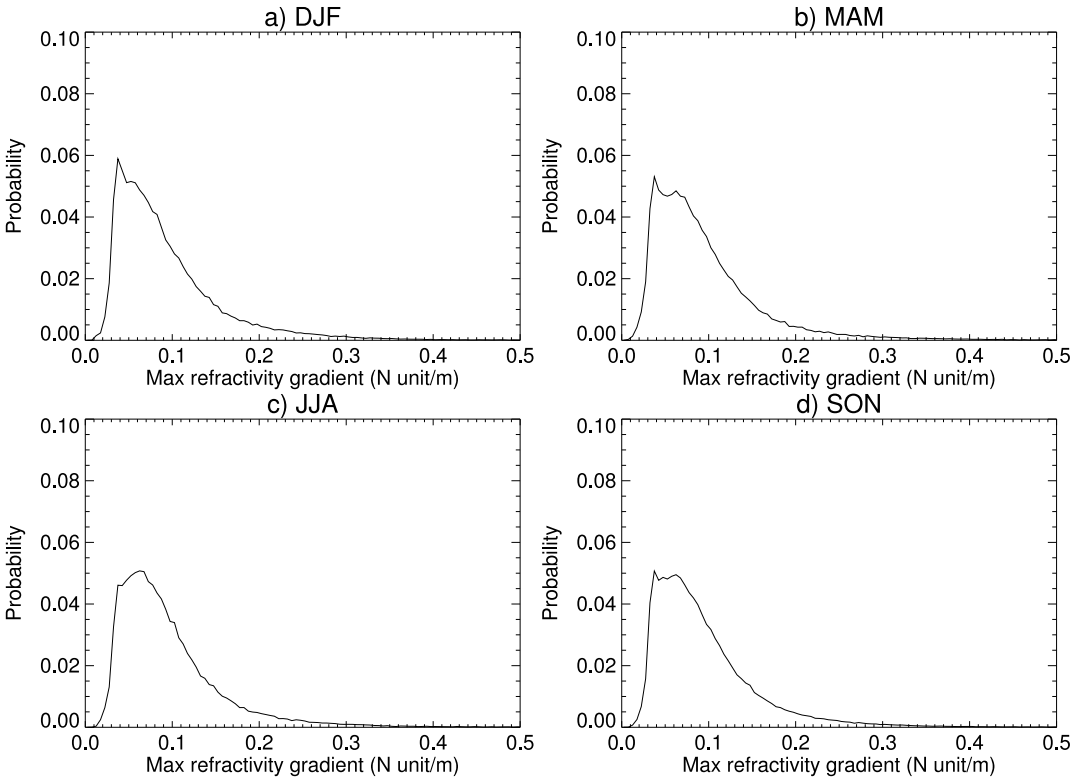

Figure 14: The globally averaged PDFs of the maximum refractivity gradient for the four seasons, spanning December 1, 2009 to November 30, 2010.

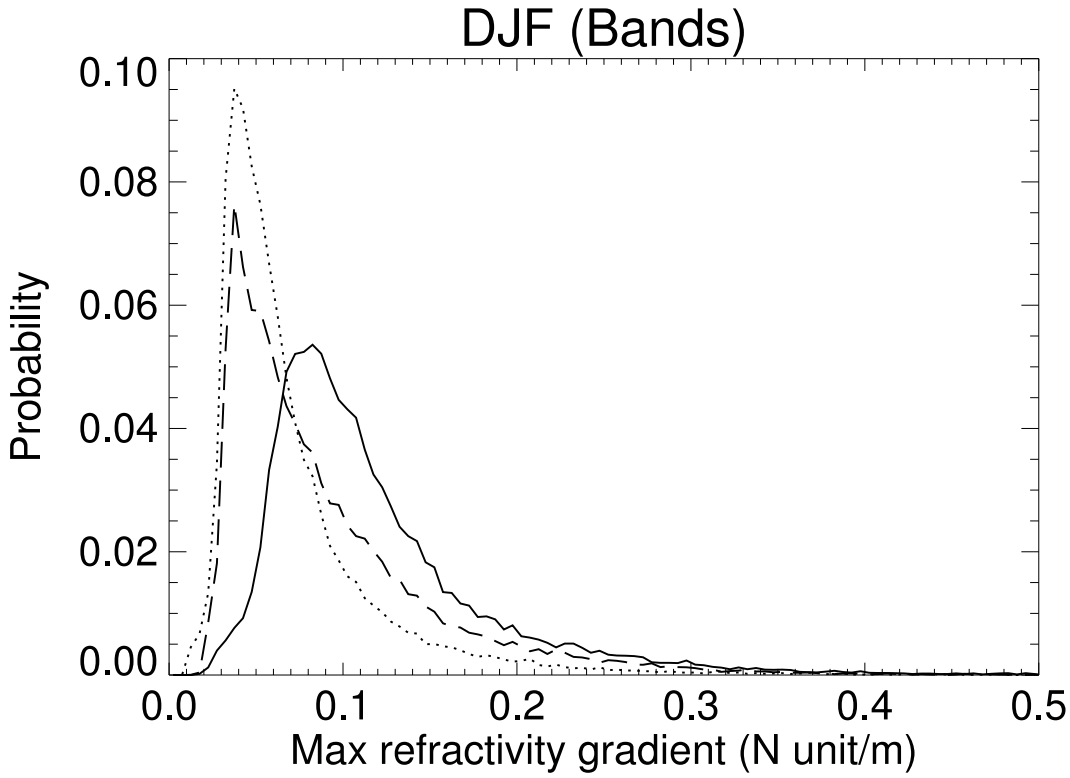

Figure 15: The PDF of the maximum refractivity gradient for the northern hemisphere extra tropics (dotted), tropics (solid) and southern hemisphere extra tropics (dashed).

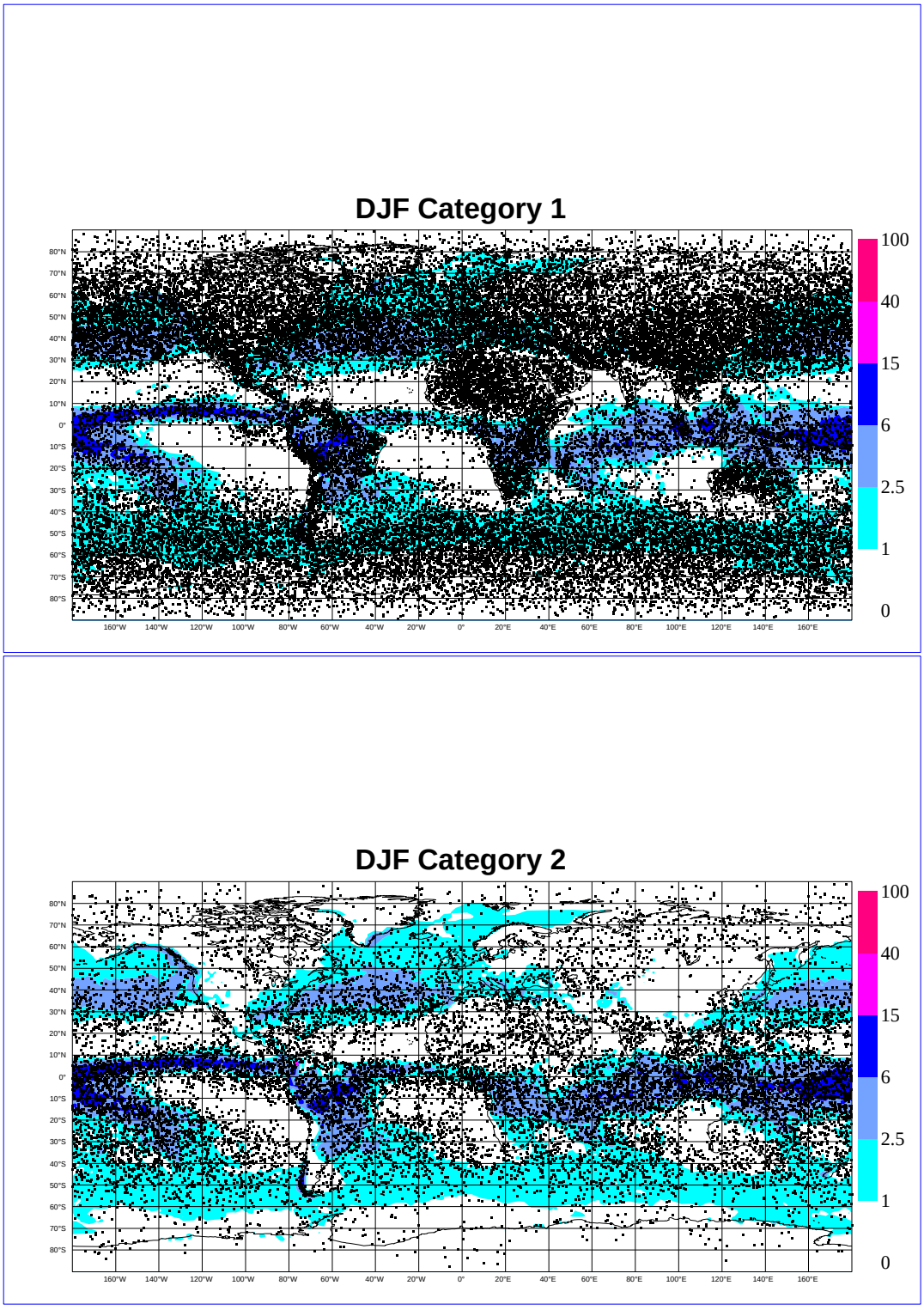

Figure 16: The spatial distribution of the category 1 and category 2 profiles, super-imposed on the total precipitation accumulated over 6 hours (mm), averaged over the DJF season.

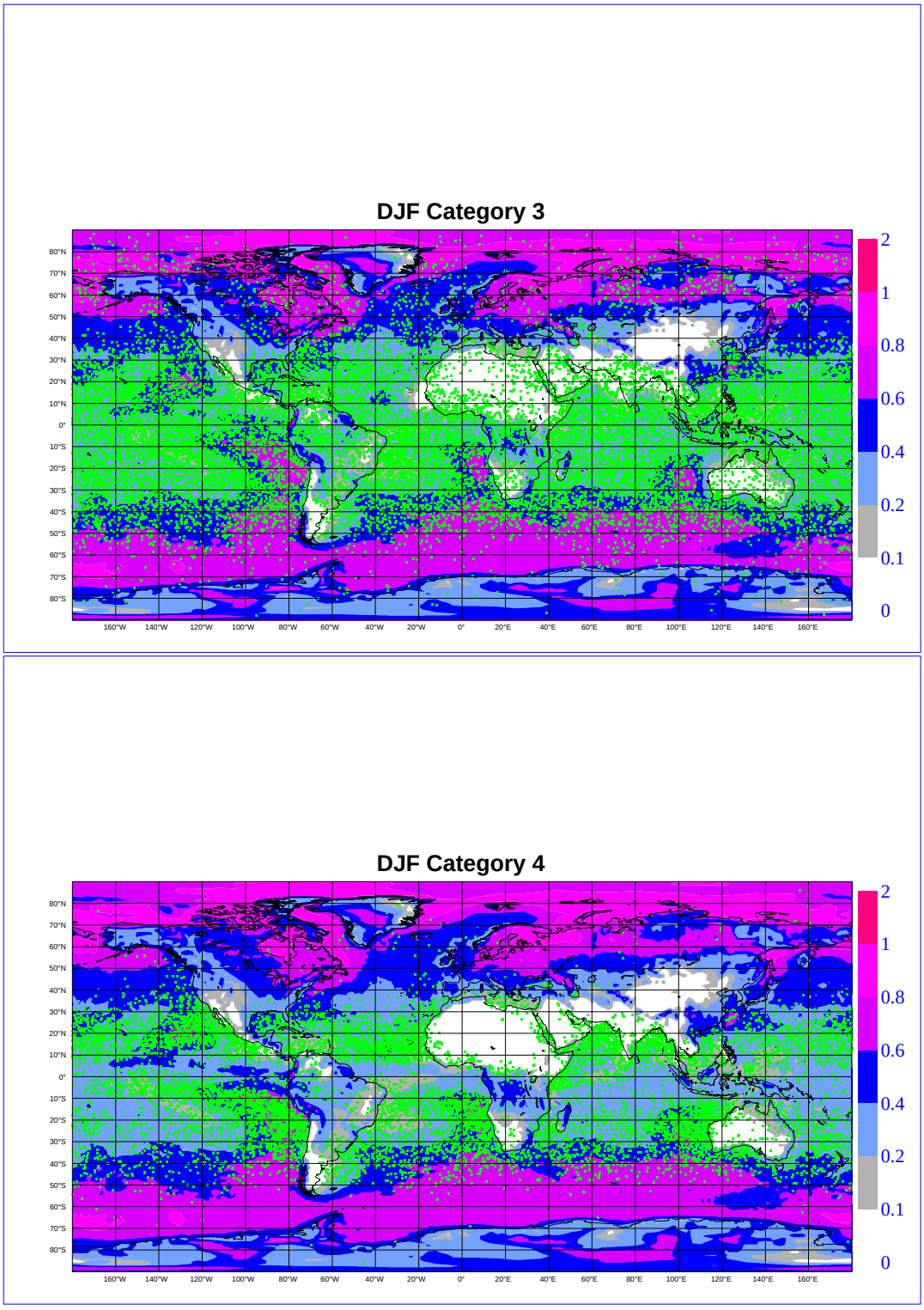

Figure 17: The spatial distribution of the category 3 and category 4 profiles, super-imposed on low cloud fraction, averaged over the DJF season. The cloud fraction is a scalar varying between 0 (cloud free) and 1 (total cloud cover).

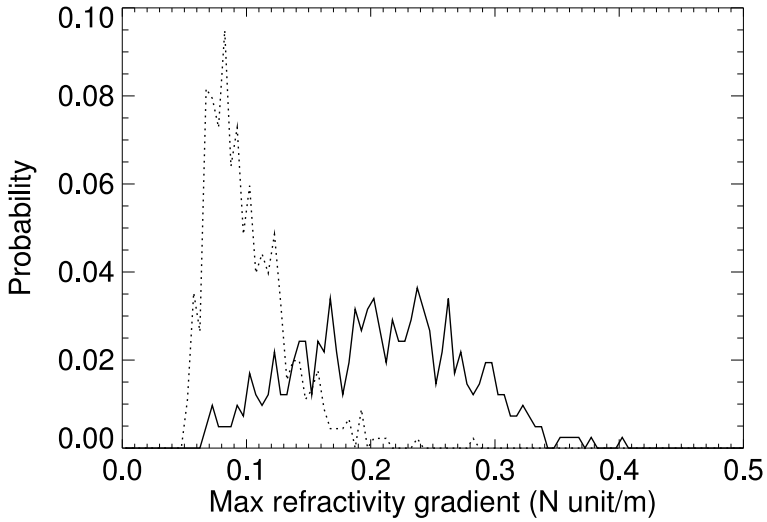

Figure 18: The PDF of maximum refractivity gradients in Area 1 (solid) and Area 2 (dotted).

5 Two-dimensional aspects

As noted in section 2, the 1D refractivity profile dataset is useful because it should be possible to forward model to phase and amplitude using a wave optics propagator, and then invert this information initially to bending angle as a function of impact parameter, $\alpha(a)$, and then back to a refractivity profile using an Abel transform. Ideally, the refractivity derived with the Abel transform should agree with the original refractivity profile used in the wave optics simulations, so the consistency of the solutions of the forward and inverse problems can be tested. However, GPS-RO measurements are two-dimensional limb measurements. The horizontal scale-length of a measurement can be estimated to first order by assuming that the atmospheric refractivity falls exponentially with height, with a scale height of ~ 6 km. This implies a Gaussian horizontal weighting function, where approximately 68% of the bending takes place over a 400 km section of path, centred on the tangent point location. It is therefore useful to quantify how horizontal variations of the refractivity might affect the signal propagation. For example, it may be that some sharp vertical gradients have a limited extent in the horizontal, and the wave optics calculations with the 1D profiles overestimate the signal de-focusing.

A dataset of 2D slices of the NWP model atmosphere, corresponding to the 1D profiles, has been constructed. The slice is defined by the representative location of the observation used in the 1D profile selection (section 2), and the azimuthal angle of the occultation, which is usually given in the header of the operational BUFR file. The azimuthal angle defines the angle of the 2D plane relative to north. Each 2D slice contains a set of 121 profiles separated by 25 km in the horizontal, so the total width of the slice is 3000 km. The refractivity of each profile within the slice is calculated using equation 1. Note that the central profile of a slice – profile number 61 – is the refractivity profile information used in the corresponding 1D file.

The ROPP 2D bending angle operator (Healy *et al.* 2007) has been used to simulate the bending angles for each slice. This calculation is based on a numerical solution of the differential equations defining the ray-path in circular polar co-ordinates (r and θ) (e.g., page 149, Rodgers, 2000)

$$\frac{dr}{ds} = \cos\phi \tag{6}$$

$$\frac{d\theta}{ds} = \frac{\sin\phi}{r} \tag{7}$$

$$\frac{d\phi}{ds} \simeq -\sin\phi \left[\frac{1}{r} + \left(\frac{\partial n}{\partial r}\right)_\theta\right] \tag{8}$$

where s is the distance along the ray-path, n is the refractive index, ϕ is angle between the local radius vector and the tangent to the ray-path. The forward model also evaluates the change of the actual impact parameter, $a = nr\sin\phi$, along the ray path

$$\frac{d(nr\sin\phi)}{ds} = \left(\frac{\partial n}{\partial \theta}\right)_r \tag{9}$$

The ROPP 2D operator currently contains two important approximations, which have relevance to this work. Firstly the bending angle calculation is started from the assumed tangent location, rather than one of the satellites, and no attempt is made to find a ray path that intersects the satellites. The second major assumption is that the tangent height used in the observation operator, r_t, is derived from the impact parameter provided with the observation, a, using $r_t = a/n_t$, where n_t is the refractive index at the tangent point derived from the NWP model state. In reality, the "observed" impact parameter, a, is related to the $nr\sin\phi$ values at the GPS and LEO satellites, rather than the value at the tangent point location, and this is a source of forward model error. It can be shown that the "observed" impact parameter provided with the observation is,

$$a = \gamma a_l + (1-\gamma)a_g \tag{10}$$

where a_l and a_g are the values of $nr\sin\phi$ at the LEO and GPS, respectively. The scalar is related to the measurement geometry and it is typically $\gamma \sim 0.85$ for realistic orbits (Healy 2001), and $\gamma = 1$ in the limit where the GPS satellite is assumed to be stationary. This incorrect tangent height assignment is also made in the 1D operator, and therefore it cancels out when looking at simulated (2D minus 1D) bending angle differences, so these can be misleading when investigating the impact of horizontal gradients. Therefore, we suggest that the variation of $a = nr\sin\phi$ along the ray-path is a more appropriate variable to analyse when investigating the impact of horizontal gradients. We provide $(a_g - a)$ and $(a_l - a)$ estimates by calculating $nr\sin\phi$ at the endpoints of the simulated ray-path.

Table 3, given in the appendix, lists the largest difference between the $nr\sin\phi$ product at the ray endpoints and the impact parameter value, a, used to calculate the tangent point height, for each profile. The sign of the difference depends on the direction of the ray-path through the gradients and it is not important here; the magnitude of the difference is related to the size of the gradient integrated along the ray-path. The differences include -17 m for CASE 52, and 273 m for CASE 16. The horizontal refractivity gradients in the 3000 km plane for these cases are shown in Figure 19. It is evident that CASE 52 has much smoother gradients than CASE 16. We believe that the information in Table 3 will provide a useful indicator as to whether horizontal gradients are likely to be an important error source in the retrieved bending angles. However, this is essentially a retrieval error, it is not clear whether large horizontal gradients and impact parameter differences imply that the phase and amplitudes at the receiver will be more difficult to measure. This will have to be investigated.

6 Concluding Remarks

A dataset of 1D profiles and 2D slices at 54 GPS-RO observation locations has been produced. The dataset should be suitable for advanced wave optics simulations. The locations have been selected to include a significant number of challenging conditions.

We have suggested four profile categories for the 1D profiles, based on the maximum refractivity gradient found above 100 m. The PDFs and spatial distribution of the categories produced by the ECMWF model have been investigated and presented. The most challenging category 3 and category 4 profiles account for around 24 %

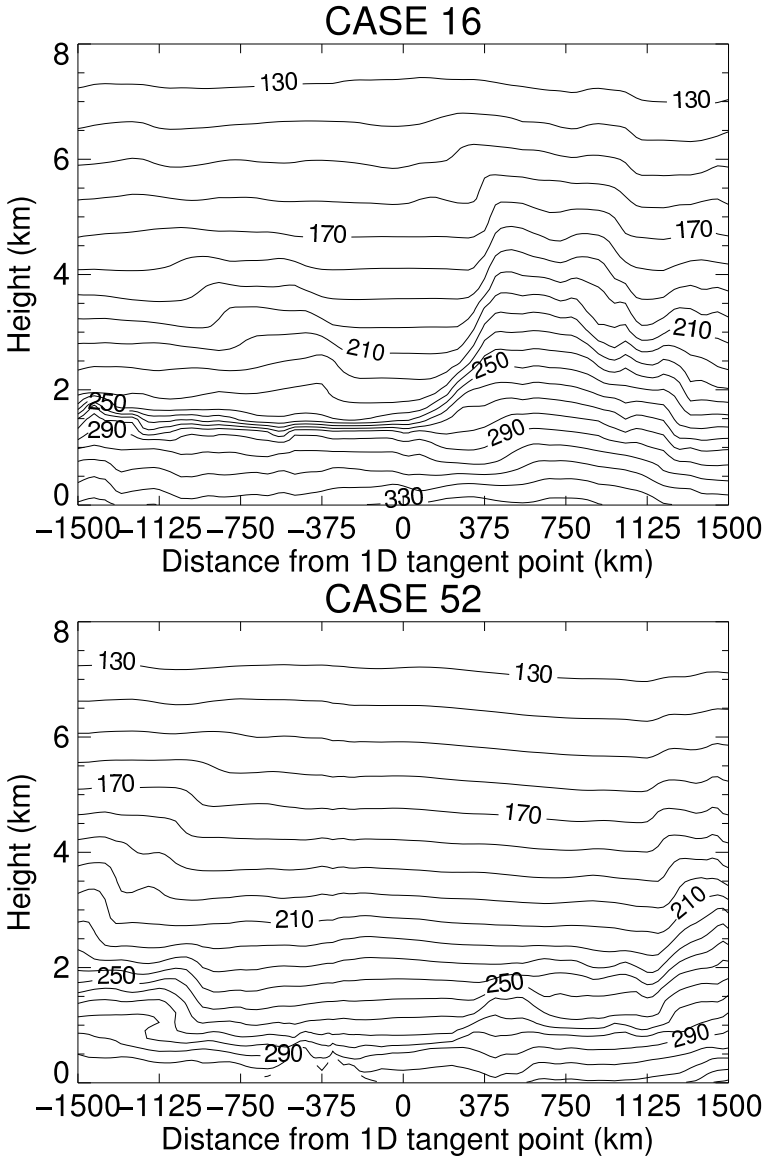

Figure 19: The cross section of the refractivity for Case 16 and Case 22, which have the largest and smallest impact parameter variation, respectively. The contours are separated by 10 N units, and 0 km in the horizontal is the location used in the 1D simulation.

and 13 %, respectively, when averaged over the globe. They tend to occur most frequently at low latitudes in low cloud conditions, rather than high water vapour. The low cloud is produced by large scale descent in this produces sharp gradients in the bending angle, resulting in significant de-focusing and probable multipath. Conversely, the easier category 1 and category 2 profiles occur most often at high latitudes, but they also arise in the tropics in convective regions. It appears that in the 1D profile approximation convection produces relatively smooth profiles of refractivity and, therefore, bending angle.

The inclusion of the 2D slices enables the impact of horizontal gradients to be investigated. It is suggested that the change in impact parameter along the ray-path (Table 3) can be used to identify cases where horizontal gradients are likely to cause large retrieval errors. However, it is unclear whether horizontal gradients produce more difficult measurement conditions for the receiver, and this should be investigated.

References

Hannay, C. *et al.*, 2009: Evaluation of forecasted Southeast Pacific stratocumulus in the NCAR, GFDL, and ECMWF models. *J. Climate*, **22**, 2871–2889.

Haugstad, B., 1978: Effect of the inhogeneous background on radiation propagating through turbulent planetary atmospheres. *Radio Sci.*, **13**, 435–440.

Healy, S., 2001: Radio occultation bending angle and impact parameter errors caused by horizontal refractive index gradients in the troposphere: A simulation study. *J. Geophys. Res.*, **106**, 11875–11889.

Healy, S., J. Eyre, M. Hamrud, and J.-N. Thépaut, 2007: Assimilating GPS radio occultation measurements with two-dimensional bending angle observation operators. *Quart. J. Roy. Meteorol. Soc.*, **133**, 1213–1227.

Healy, S., and J.-N. Thépaut, 2006: Assimilation experiments with CHAMP GPS radio occultation measurements. *Quart. J. Roy. Meteorol. Soc.*, **132**, 605–623.

Köhler, M., M. Ahlgrimm, and A. Beljaars, 2011: Unified treatment of dry convective and stratocumulus-topped boundary layers in the ECMWF model. *Quart. J. Roy. Meteorol. Soc.*, **137**, 43–57.

Rodgers, C., 2000: *Inverse methods for atmospheric sounding: Theory and practice*. World Scientific Publishing, Singapore, New Jersey, London, Hong Kong.

Sokolovskiy, S., 2003: Effect of superrefraction on inversions of radio occultation signals in the lower troposphere. *Radio Sci.*, **38**, 1058, doi:10.1029/2002RS002728.

von Engeln, A., and J. Teixeira, 2004: A ducting climatology derived from ECMWF global analysis fields. *J. Geophys. Res.*, **109**, D18104, doi:10.1029/2003JD004380, 2004.

Wyant, M. *et al.*, 2010: The PreVOCA experiment: modeling the lower troposphere in the Southeast Pacific. *Atmos.Chem.Phys.*, **10**, 4757–4774.

Xie, F., D. Wu, C. Ao, E. Kursinski, A. Mannucci, and S. Syndergaard, 2010: Super refraction effects on GPS radio occultation refractivity in marine boundary layers. *Geophys. Res. Lett.*, **37**, L11805, doi:10.1029/2010GL043299.

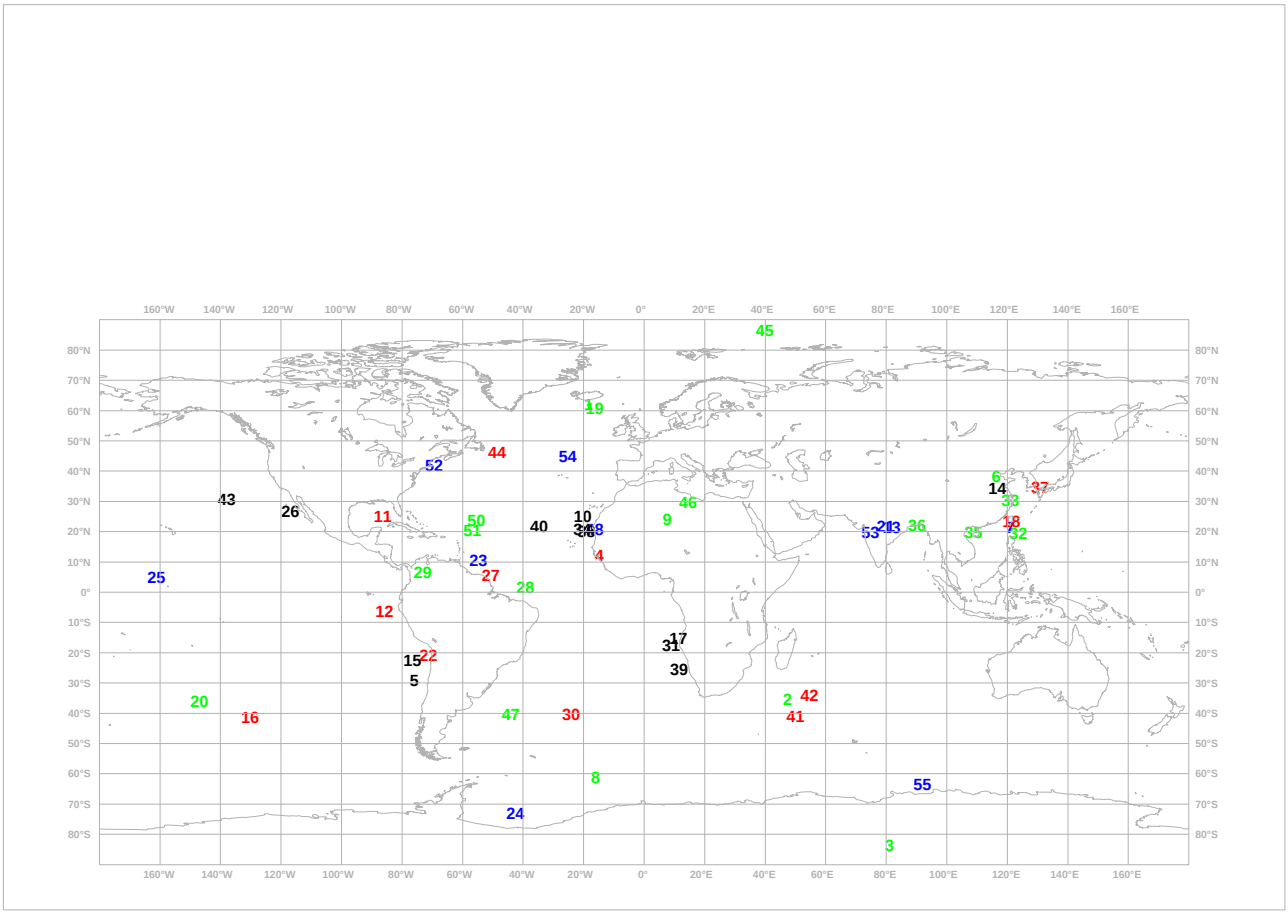

Figure 20: The spatial distribution of the seleced cases. Category 1 are shown in green, Category 2 are blue, Category 3 are red and Category 4 are black.

Appendix

A The Profile Dataset

The profile data set is listed in Table 2. The spatial distribution of the selected cases are shown in Figure 20. The change in maximum change impact parameter caused by horizontal gradients is given in Table 3.

Two errors in the original data set should be noted. Firstly, CASE 40 and CASE 49 are identical measurements, so only one should be used. Both case 40 and 49 are still included in Table 2 to preserve the numbering convention used in other work packages.

In addition, the 1D dataset originally contained two CASE 53's. Only the correct CASE 53 is now listed in Table 2.

Table 2: The first 25 cases in the 1D profile dataset

Name	WMO Satellite identifier	Date	Time (UTC, hhmmss)	lat (deg)	lon (deg)	Category
CASE_01	742	20100702	005103	62.22	-18.36	1
CASE_02	745	20100701	111850	-35.44	47.51	1
CASE_03	4	20100701	114419	-83.40	81.18	1
CASE_04	740	20100701	115259	12.43	-14.83	3
CASE_05	742	20100701	115902	-29.06	-75.84	4
CASE_06	4	20100701	120755	38.41	116.39	1
CASE_07	4	20100701	121607	21.40	121.10	2
CASE_08	742	20100701	122734	-61.12	-16.06	1
CASE_09	743	20100701	124358	24.17	7.71	1
CASE_10	743	20100701	125339	25.26	-20.34	4
CASE_11	744	20100701	235625	24.95	-86.34	3
CASE_12	744	20100701	235317	-6.37	-85.90	3
CASE_13	742	20100701	231607	21.47	81.91	2
CASE_14	740	20100701	233043	34.47	116.75	4
CASE_15	742	20100702	111659	-22.46	-76.51	4
CASE_16	741	20100702	122723	-41.31	-130.25	3
CASE_17	743	20100702	124305	-15.25	11.41	4
CASE_18	4	20100702	115522	23.50	121.42	3
CASE_19	742	20100702	235621	60.65	-16.38	1
CASE_20	743	20100703	002106	-35.80	-146.90	1
CASE_21	744	20100703	125841	21.75	79.79	2
CASE_22	744	20100703	115446	-20.74	-71.30	3
CASE_23	4	20100703	120252	10.54	-54.76	2
CASE_24	4	20100703	123907	-73.07	-42.51	2
CASE_25	743	20100703	125037	5.14	-161.06	2

Table 2: The 1D profile dataset continued

Name	WMO Satellite identifier	Date	Time (UTC, hhmmss)	lat (deg)	lon (deg)	Category
CASE_26	744	20100704	002905	26.89	-116.80	4
CASE_27	740	20100703	234052	5.47	-50.68	3
CASE_28	4	20100704	005803	1.62	-39.12	1
CASE_29	4	20100704	005913	6.46	-73.14	1
CASE_30	4	20100704	115443	-40.39	-24.15	3
CASE_31	743	20100704	114806	-17.67	8.98	4
CASE_32	4	20100704	125412	19.55	123.71	1
CASE_33	4	20100704	111409	30.30	121.08	1
CASE_34	4	20100704	115047	20.81	-20.46	4
CASE_35	744	20100721	210620	19.78	108.79	1
CASE_36	741	20100721	212016	22.05	90.12	1
CASE_37	743	20100722	130452	34.62	130.82	3
CASE_38	743	20100722	115640	20.07	-19.05	4
CASE_39	745	20100722	121148	-25.43	11.59	4
CASE_40	743	20100722	114349	21.82	-34.72	4
CASE_41	740	20100722	111813	-41.12	49.97	3
CASE_42	741	20100722	112647	-33.91	54.64	3
CASE_43	744	20100722	121513	30.83	-137.84	4
CASE_44	4	20100722	115834	46.16	-48.60	3
CASE_45	4	20100722	120017	86.56	39.99	1
CASE_46	741	20100722	112052	29.67	14.51	1
CASE_47	4	20100722	123640	-40.32	-44.04	1
CASE_48	4	20100722	120448	20.80	-16.30	2
CASE_49	743	20100722	114349	21.82	-34.72	4
CASE_50	744	20100825	235214	23.75	-55.30	1
CASE_51	4	20100916	124640	20.72	-56.80	1
CASE_52	743	20100123	233806	41.79	-69.40	2
CASE_53	740	20100123	232651	19.74	74.69	2
CASE_54	745	20100123	231220	45.00	-25.25	2
CASE_55	744	20100123	231028	-63.52	92.02	2

Table 3: The maximum change in impact parameter caused by horizontal gradients integrated along the ray-path

Name	Change in impact parameter (m)
CASE_01	-152.05
CASE_02	-111.99
CASE_03	-12.11
CASE_04	-141.97
CASE_05	-27.03
CASE_06	-403.02
CASE_07	93.44
CASE_08	58.68
CASE_09	40.12
CASE_10	-76.25
CASE_11	-72.61
CASE_12	-188.19
CASE_13	-125.88
CASE_14	73.20
CASE_15	23.18
CASE_16	272.73
CASE_17	-61.64
CASE_18	-259.88
CASE_19	-44.42
CASE_20	67.13
CASE_21	-105.80
CASE_22	-196.73
CASE_23	-66.23
CASE_24	28.17
CASE_25	-189.99

Table 3: The maximum change in impact parameter caused by horizontal gradients integrated along the ray-path continued.

Name	Change in impact parameter (m)
CASE_26	-83.72
CASE_27	53.65
CASE_28	-46.68
CASE_29	-94.13
CASE_30	91.56
CASE_31	40.81
CASE_32	-99.63
CASE_33	-257.15
CASE_34	-64.36
CASE_35	-101.50
CASE_36	-49.37
CASE_37	-77.61
CASE_38	-46.44
CASE_39	-66.35
CASE_40	-43.81
CASE_41	-36.44
CASE_42	-111.92
CASE_43	224.73
CASE_44	192.49
CASE_45	63.91
CASE_46	119.86
CASE_47	-137.41
CASE_48	-260.49
CASE_49	-43.81
CASE_50	64.24
CASE_51	-133.05
CASE_52	-16.88
CASE_53	67.39
CASE_54	113.42
CASE_55	50.29